Off-axis electron holography of bacterial cells and magnetic nanoparticles in liquid

Tanya Prozorov [1]*, Trevor P. Almeida [2†], András Kovács [3] and Rafal E. Dunin-Borkowski,[3]*

[1] Division of Materials Sciences and Engineering, Ames Laboratory, Ames IA, 50011, USA

[2] Department of Earth Science and Engineering, Imperial College London, South Kensington Campus, London SW7 2AZ, UK

[†]Present address: School of Physics and Astronomy, University of Glasgow, Glasgow G12 8QQ, UK

[3] Ernst Ruska-Centre for Microscopy and Spectroscopy with Electrons and Peter Grünberg Institute, Forschungszentrum Jülich, 52425 Jülich, Germany

Abstract

The mapping of electrostatic potentials and magnetic fields in liquids using electron holography has been considered to be unrealistic. Here, we show that hydrated cells of *Magnetospirillum magneticum* strain AMB-1 and assemblies of magnetic nanoparticles can be studied using off-axis electron holography in a fluid-cell specimen holder within the transmission electron microscope. Considering that the holographic object and reference wave both pass through liquid, the recorded electron holograms show sufficient interference fringe contrast to permit reconstruction of the phase shift of the electron wave and mapping of the magnetic induction from bacterial magnetite nanocrystals. We assess the challenges of performing *in situ* magnetization reversal experiments using a fluid cell specimen holder, discuss approaches for improving spatial resolution and specimen stability, and outline future perspectives for studying scientific phenomena, ranging from interparticle interactions in liquids and electrical double layers at solid-liquid interfaces to biomineralization and the mapping of electrostatic potentials associated with protein aggregation and folding.

Keywords

Off-axis electron holography, liquid cell TEM, magnetic nanoparticles, magnetotactic bacteria

Introduction

The localized study of electromagnetic fields in biological systems has been largely unexplored, largely due to a lack of suitable characterization techniques across a wide range of length scales. Medical applications include the use of pulsed electric or magnetic fields to treat pain relief, musculoskeletal trauma and vascular and endocrine disorders [1,2]. Electric and magnetic fields have been shown to play a significant role at the cellular and subcellular level, for example in plasma membranes and actin filaments [3,4], as well as in processes such as biomineralization, magnetotaxis [5,6] and magnetoreception [7]. A key example is the influence of electric fields on protein conformation, which has been described using theoretical models [8-10] and observed experimentally [11-14]. Charge redistribution and localization in proteins, which can be inferred using spectroscopic and computational approaches, is crucial to understanding the dynamics of protein self-assembly, aggregation and folding [3,8,15-18]. The development of an experimental technique that is capable of visualizing electromagnetic fields and measuring experimental maps of charge density and magnetization in biological organisms in liquids with sub-micron spatial resolution would advance many fields of science, from nanotechnology to bioimaging.

The ability to map electrostatic potentials and magnetic fields on the nanoscale is provided by the advanced transmission electron microscope (TEM) technique of off-axis electron holography. This method involves the use of an electrostatic biprism to facilitate the overlap of an electron wave passed through an electron-transparent specimen with a reference wave that has passed through vacuum alone. Analysis of the resulting interference fringe pattern provides access to both low and high spatial frequencies of the phase shift of the electron wave that has passed through the specimen. The phase shift is, in turn, sensitive to electrostatic potentials and magnetic fields within and around the specimen, projected in the electron beam direction. The electrostatic contribution to the phase shift includes contributions from both longer-range charge redistribution and the electrostatic potentials of the constituent atoms, whose spatial average is referred to as the mean inner potential (MIP).

The phase shift can be represented as a sum of electrostatic and magnetic contributions in the form

$$\varphi(x,y) = \varphi_e + \varphi_m = C_E \int V(x,y,z)dz - C_B \int A_Z(x,y,z)dz, \quad (1)$$

where $C_E = \pi\gamma/\lambda U^*$ is an interaction constant that depends on the accelerating voltage of the electron microscope (C_E = 6.53 V^{-1} μm^{-1} for 300 kV electrons), λ is the electron wavelength, γ is the relativistic Lorentz factor and U^* is the relativistically corrected accelerating potential [191], while the constant $C_B = \pi/\phi_0$, where ϕ_0 is the magnetic flux quantum $h/2e = 2.07\times10^3$ T nm^2, is independent of the electron energy [19]. When examining magnetic fields in materials, the electrostatic contribution to the phase is almost always regarded as an unwanted perturbation. However, it usually cannot be neglected because of the MIP of the material.

Off-axis electron holography has primarily been used by physicists and materials scientists, with only a small number of reports of the application of the technique to biological objects [20-22]. Measurements of the MIP contribution to the phase shift of biological samples using off-axis electron holography can in principle be used to study weakly scattering materials, providing the possibility to enhance contrast by implementing phase plates in software after

hologram acquisition and reconstruction, thereby eliminating the need for defocusing or staining techniques or hardware phase plates [3,23-25]. However, experimental reports are scarce, in part because of difficulties associated with preparing an optimal specimen geometry and electron-beam-induced damage, charging and contamination [38,41-43]. As the phase shift of the electron wave is small for biological specimens, the examination of biological objects using off-axis electron holography can also require a higher electron dose than for inorganic materials [24,27,29]. Moreover, in order to accumulate an adequate phase shift, the specimen generally has to be thicker, leading to increased inelastic scattering and background noise, which can be detrimental to specimen integrity and can result in the need to use an energy filter in addition to an electrostatic biprism [24,27].

Despite being susceptible to radiation damage, a number of unstained biological specimens have been studied successfully using off-axis electron holography in the TEM, including ferritin, tobacco mosaic virus and protein S-layers [23,24,30]. In-line low-energy electron holography has also been used to study DNA, bacteriorhodopsin, tobacco mosaic virus and collagen with nanometer spatial resolution [29,31,32]. However, at low electron energies the MIP contribution to the phase shift increases relative to the magnetic contribution, complicating measurements of nanoscale magnetic fields significantly. It should be noted that, in addition to off-axis and in-line electron holography, other phase contrast techniques such as ptychography [33-37], diffractive imaging [38-40] and differential phase contrast imaging [41-43] are also potentially applicable to studies of soft and biological materials. The majority of studies of biological materials in the TEM are currently carried out in the absence of a liquid environment. Although the high vacuum of the electron microscope makes standard imaging of such specimens in their native hydrated state impossible [28], recent advances in fluid cell TEM specimen holder technology are providing new opportunities for the *in situ* characterization of dynamic processes in liquids with sub-nanometer spatial resolution [44], with recent reports describing studies of inorganic nanoparticles, biomimetic structures, protein molecules [45-48], eukaryotic cells [44,49,50] and bacteria [51]. Whilst experimental approaches for the high-resolution *in situ* characterization of specimens in liquid are becoming capable of imaging structures and monitoring their dynamic properties, measurements of electromagnetic fields in such specimens have not yet been performed, in part because *electron holography in liquid* as an experimental technique has been assumed to be difficult and impractical [52]. With the exception of a recent report on the application of electron holography to ionic liquids [53], no other applications of electron holography to liquid samples or using a fluid cell specimen holder are yet available.

Here, we present a proof-of-principle off-axis electron holography study of both intact and fragmented cells of magnetotactic bacterial strain *Magnetospirillum magneticum* AMB-1 in liquid. Magnetotactic bacteria biomineralize ordered chains of magnetite or greigite nanocrystals with nearly perfect crystal structures and strain-specific morphologies. These microorganisms have been established as one of the best model systems for investigating the mechanisms of biomineralization. The biogenic magnetite crystals that they form have crystal habits and properties that have been studied in great detail. Furthermore, the magnetic fields that are associated with ferrimagnetic nanocrystal chains biomineralized by magnetotactic bacteria have been visualized using off-axis electron holography [6,21,54-56]. We selected this specimen based on extensive reports of the characterization of the chemistry and magnetism of magnetotactic bacteria by a variety of methods [57-59], as well as on our own report on imaging viable bacterial cells in liquid using an *in situ* fluid cell TEM specimen holder [51]. We begin by measuring the remanent

saturation magnetization of magnetite nanoparticles located both within and outside hydrated bacterial cells. We also estimate the MIP of the liquid in the fluid cell holder.

Results

Figure 1 shows schematic diagrams of the experimental setup for TEM imaging using a fluid cell (**Fig. 1A**) and off-axis electron holography (**Fig. 1B**). Upon assembly of the fluid cell, a small amount of liquid is sandwiched between two electron-transparent SiN membranes. When examining bacterial cells, the microorganisms and surrounding growth medium are trapped by the windows, resulting in a mechanical stress on the bacterial cell walls. In the present study, the holographic reference wave was usually obtained through a layer of liquid, in addition to passing through two 50-nm-thick layers of SiN. The chemical composition of the liquid present, its estimated thickness and the hologram acquisition parameters are given in the Materials and Methods.

Figure 2A shows an off-axis electron hologram of a bacterial specimen in a liquid cell, while **Fig. 2B** shows a corresponding reconstructed (wrapped) phase image. Since the phase shift is dominated by the MIP contribution to the phase, it represents the thickness profile of the specimen in a confined geometry, with the bacterial cell located between the SiN membranes and the liquid present on both sides of it. It should be noted, however, that the phase image contains features arising from the holographic reference wave, which was also acquired from a liquid-containing region of the sample. The reconstructed amplitude image is shown in **Fig. 2C** and is consistent with the presence of an enclosed bacterial cell. **Figures 2D-F** show a region extracted from the off-axis electron holograms of the hydrated bacterial cell recorded in its initial state (**Fig. 2D**), after tilting by +75° and applying a magnetic field in the direction of the electron beam (**Fig. 2E**) and after tilting by -75° and applying a magnetic field of the same magnitude and direction (**Fig. 2F**). The left side of the image changes between **Fig. 2D and Fig. 2F** as a result of electron-beam-induced changes to the liquid, which are indicated in the form of a progression of voids, become more pronounced with cumulative exposure time and can be used to verify the presence of liquid. Significantly, the bacterial cell wall does not appear to have ruptured, as evidenced by the bacterial body maintaining its integrity and shape, as well as its relatively constant density during imaging. The cell wall may correspond to the bright band that is visible around the periphery of the cell in the phase image shown in **Fig. 2B**. **Figure 2G** shows a relevant part of a magnetic induction map recorded from the magnetite nanocrystal chain in the bacterial cell. The individual magnetite nanocrystals are outlined in white, while the direction of the projected in-plane magnetic induction is indicated using arrows and colors. For clarity, the phase contours have been obscured on the left side of the image, which contains artifacts associated with the electron-beam-induced bubbling of the liquid. The magnetic induction map in **Fig. 2G**, which was determined from the magnetic contribution to the phase shift reconstructed from the electron holograms shown in in **Figs 2E** and **2F**, provides a quantitative representation of the magnetic field in the magnetite nanocrystals, which each contain a single magnetic domain, as well as the stray magnetic field around them. **Fig. 2H** shows a profile of the magnetic contribution to the phase image that was used to create **Fig. 2G**, taken along the red dashed line passing through the center of the crystal, perpendicular to the phase contours. The phase profile was then used to estimate the in-plane magnetic induction across the particle, using a previously described method [62]. To achieve this, the particle was treated as a sphere and the difference between the maximum

and minimum values of the magnetic contribution to the phase shift were substituted into the equation: $\Delta\varphi_{mag} = 2.044(e/h)B_{\perp}a^2$, where e is the magnitude of electronic charge, $\hbar$ is reduced Planck's constant, a is the particle's radius and $B_{\perp}$ is the in-plane magnetic induction. In the case for spherical particles, the measured $B_{\perp}$ is only 2/3 of the saturated magnetic induction and after including this correction, the latter was estimated as 0.58 ± 0.1 T, which is consistent with the room temperature saturation induction of magnetite [62].

Figure 3 shows an off-axis electron hologram and a corresponding magnetic induction map recorded from a magnetite nanocrystal chain that had been released from a ruptured bacterium inside the fluid cell. When compared to the hydrated bacterium shown in **Fig. 2**, the Michelson contrast ratio increases from ~ 15% to ~ 30% and the spatial resolution is improved, presumably due to the absence of the protoplasm and cellular compartments seen in **Fig. 2**. The magnetic induction map shown in **Fig. 3B** again provides a quantitative representation of the magnetic field in the magnetite grains and their magnetostatic interactions. In a similar fashion to **Fig. 2H**, **Fig. 3C** shows a profile of the magnetic contribution to the phase image, taken along the red dashed line passing through the center of the crystal in **Fig 3B**. A saturated magnetic induction of 0.63 ± 0.1 T was estimated for the particle, which is again consistent with the room temperature saturation induction of magnetite [62]. The blurring of the contour lines in the lower-most crystal in **Fig. 3B** could result from the presence of a magnetic vortex domain state or a crystallographic twin, as seen in **Fig. 3A** [61]. These possibilities make the magnetic signal in this crystal difficult to interpret. The large magnetite crystal adjacent to the twinned crystal is surrounded by biological cellular material that is likely to be a remnant membrane and the liquid appears to cover only the left part of the chain.

Figures 4A and **4B** show representative off-axis electron holograms recorded from different regions of the fluid cell. **Figure 4A** was recorded from the middle of the cell, while **Fig. 4B** shows a liquid front that only partially covers the SiN window. Each electron hologram contains clear, well-resolved holographic interference fringes. **Figure 4C** shows an off-axis electron hologram of a droplet of liquid that has a diameter of ~1200 nm and is resting on the SiN window. Based on an estimate of the thickness of the liquid in a fluid cell reported elsewhere, the droplet of liquid is assumed to be somewhat compressed with a height of ~800 nm [51]. **Figure 4D** shows a radial average of the intensity of the droplet, while **Figure 4E** displays the reconstructed amplitude image of the droplet. The dark contrast of the droplet in the amplitude image confirms that it is not a bubble. The t/λ profile across the droplet was estimated from the amplitude image, using the equation $t / \lambda = - 2 \ln (A_{zl} / A_0) = - 2 \ln A_n$, where A_{zl} is the holographically reconstructed (zero-loss) amplitude, A_0 is the reconstructed amplitude from an area of no liquid and A_n is treated as the normalized amplitude. Using the maximum plotted value of $t/\lambda = 3.26$ and on the assumption that the droplet has a height of ~ 800 nm, based on the previously estimated thickness of a fluid cell with the enclosed bacterium [51], we calculated a λ value of 245 nm. **Figure 4G** shows the reconstructed phase shift across the droplet and again on the assumption of a droplet thickness of ~800 nm, the expression $V_0 = \emptyset_c(x,y)/(C_E t(x,y)$ for an accelerating voltage of 300 kV [62] was used to estimate the value for the MIP of the droplet as 3.5±0.5 V.

Figure 5 shows a comparison of off-axis electron holograms recorded using a conventional charge-couple device (CCD) camera and a Gatan K2 direct detection camera. The interference fringe contrast is improved significantly when using the K2 camera, from a Michelson contrast ratio of ~ 25% to 65 %.

Discussion

A significant challenge associated with the use of off-axis electron holography in combination with a fluid cell is the acquisition of a reference electron wave through liquid instead of vacuum. It is also challenging to obtaining a reference electron hologram from an area that is close to the region of interest. In our experiments, the reference hologram was typically acquired from the aqueous medium in a suitable area of the fluid cell that was absent of cell debris. Rapid movement of the liquid front is often reported to have been followed by the formation of voids, vapor-filled bubbles and residual hydrated islands on SiN membranes [63-65]. Due to the relatively large size of the bacteria, bright-field imaging of entire cells was typically carried out at low magnification (7000 – 15000×) [5,54,66-68]. Off-axis electron holograms were recorded at higher magnification using a reduced electron dose rate compared to that used for bright-field imaging, requiring longer acquisition times. Bacterial cells were most easily detectable near to the corner or the edge of the SiN window, where the liquid layer was thinnest because the bulging of the SiN membrane is less pronounced in these parts of the cell, resulting in the highest relative signal-to-noise ratio.

Cells of *Magnetospirillum magneticum*, strain AMB-1, are helical in shape and typically 1-3 µm in length and 400-600 nm in diameter, with the magnetite nanocrystal chains inside the cytoplasmic membrane and held together by actin-like filaments [69]. Based on our previous experiments on magnetotactic bacteria in a fluid cell using scanning TEM, the liquid layer thickness was typically 500–750 nm at the edges and corners of the SiN windows for the used spacer configuration instead of the nominal thickness of 200 nm, with the magnetite chains acting as natural high-contrast labels denoting the positions of the individual cells of *M. magneticum* (see Experimental Details) [51]. Furthermore, the arrangement of the magnetite nanocrystals in chains was indicative that the cell membrane and vesicles had remained intact [5].

In the present experiment, the alignment of the magnetite nanocrystals in chains served an indicator of the integrity of the bacterial cellular structure, as shown in **Fig. 2**. Despite electron-beam-induced displacement and partial evaporation of the liquid surrounding the bacterial cells, we observed no signs of cell wall rupture or release of the magnetite chains, suggesting that the bacteria remained in a hydrated state. However, continuous imaging at high magnification in other regions resulted in damage, as evidenced by the collapse of internal cellular structures, rupture of bacterial cell wall membranes and the release of magnetite nanocrystal chains into the surrounding liquid, followed by amorphization of individual magnetite nanocrystals (**Fig. S1**). When compared to images obtained from dried specimens, the distance between individual magnetite nanocrystals in the fluid cell was observed to have increased slightly [54,70-72]. This result is consistent with images obtained using cryo-EM [66,73] and can be attributed to the magnetosome membranes and other sub-cellular compartments remaining in a hydrated state, without the distortions that are typically introduced by the drying of biological matter.

Initial magnetic states and magnetization reversal in the fluid cell

After magnetizing the hydrated sample in opposite directions *in situ* in the electron microscope and recording electron holograms of oppositely magnetized regions of the same magnetite nanocrystals, the resulting phase images were subtracted from each other to eliminate the contribution of the MIP and hence isolate the magnetic contribution to the phase shift. In such an experiment, the MIP contribution to the phase must be identical in each pair of electron

holograms. However, prolonged exposure to the electron beam resulted in evaporation of liquid, void formation and evolution, resulting in the presence of artefacts after calculating differences between each phase image associated with the specimen being magnetized in opposing directions. In the present study, the artifacts associated with the displacement of liquid and void evolution had no apparent effect on the recorded magnetic signal in the magnetite nanocrystals and the magnetic induction map shown in **Fig. 2G** is in good agreement with previous reports of electron holographic imaging of dried bacterial specimens, with the exception of a somewhat larger distance between individual magnetite nanocrystals, which we attribute to the bacterial cell and its subcellular components remaining in a hydrated state [21,54-56,74,75]. The continuous displacement of liquid in the left part of the image can be used to gauge the residual presence of liquid in the fluid cell, whilst the bacterial cell wall does not appear to have ruptured during imaging, leaving the bacterium hydrated. For comparison, lysed bacterial cells displayed collapsed chains and shorter fragments of magnetite chain, as shown in **Fig. 3**. Although the signal-to-noise ratio is somewhat improved in the fragmented chains when compared to that recorded from an intact bacterial cell (**Fig. 2 D-F**), the magnetic induction map is consistent with that shown in **Fig. 2G**.

Despite beam-induced displacement and bubbling of the liquid, we recorded off-axis electron holograms with well-resolved interference fringes from different regions of the fluid cell, as shown in **Fig. 4**. We could then reconstruct phase images, such as that shown for a droplet in **Figs 4C-F**, even in the presence of two layers of SiN encasing the liquid in the fluid cell. Similar phase images could be used in future studies of the formation of electrical double layers at solid-liquid interfaces. From the phase image, we estimated the MIP of the liquid at 3.5±0.5V based on the assumption of a droplet height of ~800 nm, in agreement with a value predicted theoretically by Kathmann and co-workers [76-79] for the liquid-vapor interface of water, as well as with that measured experimentally for vitrified ice [80].

Electron-beam-induced damage

Whereas the use of a cumulative electron dose on the order of ~0.1 e/Å^2 has been shown to induce only small changes in cellular structure during a single scanning TEM exposure [51], the imaging conditions for off-axis electron holography typically require a higher electron dose. It has long been postulated that the ultimate resolution for biological materials will be determined by the tolerable electron dose on the specimen [24,81] and hence that mitigating radiation damage is critical for fluid cell TEM imaging, which has been shown to suffer from electron-beam-induced artifacts [63-65]. Although electron beam damage in liquids poses a serious challenge, our results demonstrate that off-axis electron holography in a fluid cell is feasible. In a separate experiment, we imaged using spot size 4 in an attempt to reduce electron beam damage to bacterial cells. This led to a decrease in the overall contrast. However, the interference fringe contrast remained sufficient for data analysis. Several bacterial cells appeared intact and showed no indications of electron beam damage (**Fig. S3**). In the future, direct detection cameras promise to allow image acquisition using shorter exposure times, thereby lowering electron beam damage to both the liquid and the hydrated specimen, as demonstrated in **Figure 5**. More systematic studies aimed at establishing the tolerable electron dose utilized in electron holographic imaging of specimens in liquid will be required. In this regard, the future use of less electron beam sensitive liquids will be beneficial.

Conclusions

We have demonstrated that off-axis electron holography can be carried out in a commercially available fluid cell TEM specimen holder through a study of hydrated bacterial cells of *M. magneticum* strain AMB-1 in a ~800-nm-thick layer of liquid. Although the liquid surrounding the bacterial cells exhibited signs of electron-beam-induced changes, which contributed to artefacts and noise, the recorded electron holograms showed sufficient interference fringe contrast to permit reconstruction of the phase shift of the electron wave and mapping of the magnetic induction of the bacterial magnetite nanocrystals. We also estimated the mean inner potential of a droplet of liquid at 3.5±0.5V, based on the assumption that the droplet height was ~800 nm.

Although the choice of liquid and the protocols for data acquisition and processing will need to be refined in the future, in the present study magnetic induction mapping of intracellular magnetite nanocrystals and shorter magnetite chain fragments in liquid was successful. We expect that this approach will be applicable to a wide variety of liquid specimens that contain nanoparticles in their native environment, free of the artefacts that are associated with common preparatory methods.

Off-axis electron holography in liquid offers great promise for studying interactions between magnetic nanoparticles, as well as for the visualization of nanoparticle response to external magnetic stimuli with nanometer spatial resolution. Prospects for other applications of *in situ* off-axis electron holography in a liquid cell include research into magnetic resonance imaging, tissue repair and targeted drug delivery. The method also promises to be applicable to other interfacial phenomena in liquids, including the direct imaging of electrochemical double layers at solid-liquid interfaces, which is of relevance to colloidal suspensions, catalysis, nanofluidic devices, batteries and tribology. Other potential applications include studies of biomineralization and the mapping of electrostatic potentials associated with protein aggregation and folding. The technique promises to open a new era in the physics of liquids by revealing what role magnetostatic and electrostatic interactions play in phase transformations, the physics of coalescence, the effects of confinement and other complex phenomena.

Materials and Methods

Fluid cell assembly: Aqueous solutions were prepared using deionized water passed through a Millipore Milli-Q Plus water purification system (ρ = 18.2 MΩ cm). *In situ* liquid cell (S)TEM experiments were carried out using a commercial fluid cell holder platform (Hummingbird Scientific, Lacey, WA, USA). The experimental setup consists of a microfluidic chamber, which takes the form of two Si chips with electron-transparent SiN windows in a hermetically-sealed TEM specimen holder[89]. Unless noted otherwise, the SiN chips were plasma-cleaned for 5 minutes prior to use to hydrophilize the surfaces and ensure contaminant removal. A thin liquid layer (typically 200-800 nm thick) was formed by sandwiching two SiN-coated Si chips with a 50 × 200 μm electron-transparent 50-nm-thick SiN opening etched from the center, thereby forming an imaging window. Both SiN windows had a 100 nm SU-8 spacer. We drop-casted 1 μL of liquid onto the top SiN window, removed the excess liquid using filter paper and topped it with the second chip to form the liquid layer. The fluid cell was hermetically sealed to prevent evaporation

of the liquid. Following cell assembly, we checked the integrity of the sealed fluid cell in vacuum, inserted the holder into the electron microscope and allowed it to equilibrate for 20 minutes before imaging.

Bacterial culture growth: Cells of *Magnetospirillium magneticum* AMB-1 (ATCC 700264) used for the *in situ* fluid cell electron holography imaging experiments were grown at room temperature under microaerobic conditions in 5 ml flasks containing the modified flask standard medium (FSM) lacking the major source of iron (ferric citrate) and only containing a small amount of iron (0.36 μM) present in the mineral solution [82-84]. We aimed at using bacterial cells with only freshly formed magnetite magnetosome nanocrystals. The non-magnetic bacterial cultures were then subcultured and FSM medium containing 50 μM ferric citrate was added to the cells grown under a low iron condition to induce magnetite biomineralization [84]. The microorganisms were sampled 60 minutes after biomineralization induction. They exhibited a somewhat lower number of magnetite nanocrystals, when compared to the use of a regular bacterial growth protocol [84].

Fluid cell TEM imaging of magnetotactic bacteria: A thin liquid layer containing the specimen was maintained between the SiN windows. As mentioned above, bacterial cells were attached to a (3-Aminopropyl)triethoxysilane (APTES) coated SiN window with a 100 nm SU-8 spacer to render it hydrophilic and positively charged [51], and paired with another 100 nm SU-8 spacer window. Previous low-loss electron energy loss spectroscopy (EELS) revealed that for the used spacer configuration the liquid layer thickness was typically 500–750 nm at the edges and corners of the SiN windows, significantly higher than the nominal thickness of 200 nm [51]. The APTES-functionalized window chips encouraged consistent attachment of cells, as described previously [51]. The cells were strongly attached and imaged at magnifications of up to 200,000 x without detachment of the bacteria from the SiN window. Preliminary imaging and characterization of the specimens using the fluid cell holder platform was carried out in an FEI Tecnai G^2 F20 (scanning) TEM operated at an accelerating voltage of 200 kV. This microscope was equipped with a Tridiem Gatan Imaging Filter, a high-angle annular dark-field detector and energy-dispersive X-ray spectroscopy, as reported elsewhere [51].

Off-axis electron holography: Off-axis electron holography experiments were carried out in an FEI Titan 80–300 (scanning) TEM operated at an accelerating voltage of 300 kV. Off-axis electron holograms were acquired in Lorentz mode on a charge-coupled device camera or Gatan K2 direct detection camera using an electron biprism operated at 90–100 V. The experiments were performed at room temperature using magnification ranging from 77,000 × to 225,000 × and an acquisition time of 6-8 s. Depending on the magnification of the electron holograms acquired, the Michelson contrast ratios of the reference wave holograms ranged from ~8% to ~30%. Similarly, the average electron count for both 6 and 8 second acquisitions ranged from 1,500 to 10,000 across the magnification range. The estimated dose rate on the specimen is given in Supplementary Material, **Table 1**.

Initial magnetic states and magnetization reversal experiments using the fluid cell: Initial magnetic states were recorded after loading the fluid cell holder into the TEM in close-to-magnetic-field-free conditions. The direction of magnetization of each magnetite nanocrystal chain was subsequently reversed *in situ* in the TEM by tilting the sample by 75° and turning on the conventional microscope objective lens to apply a magnetic field of > 1.5 T parallel to the electron beam direction. The objective lens was then turned off and the sample tilted back to 0° for

hologram acquisition in magnetic-field-free conditions. In this way, holograms were recorded with the chains magnetized in opposite directions. The approach that was used to separate the magnetic from the MIP contribution to the recorded phase shift is described elsewhere [54]. Hence, the subsequent magnetic induction maps present the remanent saturation magnetization of the magnetite chains. For reconstruction of magnetic induction maps, a chosen multiple of the cosine of the magnetic contribution to the phase shift was evaluated to produce magnetic phase contours. Colors were generated from the gradient of the magnetic contribution to the phase shift and added to the contours to show the direction of the projected induction.

Acknowledgments

The present research on *in situ* electron microscopy with a fluid cell was supported by the U.S. Department of Energy, Office of Science, Basic Energy Sciences, Division of Materials Sciences and Engineering. T.P. acknowledges support from a Department of Energy Office of Science Early Career Research Award, Biomolecular Materials Program. The work at Ames Laboratory was supported by the U.S. Department of Energy, Office of Science, Basic Energy Sciences, Division of Materials Science and Engineering. The Ames Laboratory is operated for the U.S. Department of Energy by Iowa State University under contract # DE-AC02-07CH11358. T.P. wishes to thank the laboratory of Dr. Faivre for sharing the bacterial cultures grown under low iron conditions. Off-axis electron holography was carried out in the Ernst Ruska-Centre for Microscopy and Spectroscopy with Electrons in Forschungszentrum Jülich. The research leading to these results received funding from the European Research Council under the European Union's Seventh Framework Programme (FP7/2007-2013)/ ERC grant agreement number 320832.

Author contributions: T.P. conceived the study. T.P. and T.P.A. designed and carried out the experiments. A.K. assisted with the experimental work and discussions. T.P. and T.P.A. led the writing of the paper, with contributions from A.K and R.E.D-B.

Competing interests: The Authors declare no competing interests.

References

1 Merla, C. *et al.* Microdosimetry for nanosecond pulsed electric field applications: a parametric study for a single cell. *IEEE transactions on bio-medical engineering* **58**, 1294-1302 (2011).

2 Markov, M. XXIst century magnetotherapy. *Electromagnetic biology and medicine* **34**, 190-196 (2015).

3 Fröhlich, H. The extraordinary dielectric properties of biological materials and the action of enzymes. *Proc. Nat. Acad. Sci. USA* **72**, 4211-4215 (1975).

4 Tuszyn´ski, J. A., Portet, S., Dixon, J. M., Luxford, C. & Cantiello, H. F. Ionic Wave Propagation along Actin Filaments. *Biophys. J.* **86**, 1890–1903 (2004).

5 Bazylinski, D. A. & Frankel, R. B. Magnetosome formation in prokaryotes. *Nat Rev Micro* **2**, 217-230, doi:http://www.nature.com/nrmicro/journal/v2/n3/suppinfo/nrmicro842_S1.html (2004).

6 Frankel, R. B., Dunin-Borkowski, R. E., Posfai, M. & Bazylinski, D. A. Magnetic microstructure of magnetotactic bacteria. *Handbook of Biomineralization: Biological Aspects and Structure Formation*, 127-144 (2007).

7 Lang, C., Schüler, D. & Faivre, D. Synthesis of Magnetite Nanoparticles for Bio- and Nanotechnology: Genetic Engineering and Biomimetics of Bacterial Magnetosomes. *Macromolecular Bioscience* **7**, 144-151, doi:10.1002/mabi.200600235 (2007).

8 Budi, A., Legge, F. S., Treutlein, H. & Yarovsky, I. Electric Field Effects on Insulin Chain-B Conformation. *Journal of Physical Chemistry B* **109**, 22641-22648, doi:10.1021/jp052742q (2005).

9 Toschi, F., Lugli, F., Biscarini, F. & Zerbetto, F. Effects of Electric Field Stress on a β-Amyloid Peptide. *Journal of Physical Chemistry B* **113**, 369-376, doi:10.1021/jp807896g (2009).

10 Xie, Y., Pan, Y., Zhang, R., Liang, Y. & Li, Z. Modulating protein behaviors on responsive surface by external electric fields: A molecular dynamics study. *Applied Surface Science*, Ahead of Print, doi:10.1016/j.apsusc.2014.11.078 (2014).

11 Bekard, I. & Dunstan, D. E. Electric field induced changes in protein conformation. *Soft Matter* **10**, 431-437, doi:10.1039/c3sm52653d (2014).

12 Beyer, C., Christen, P., Jelesarov, I. & Froehlich, J. Experimental system for real-time assessment of potential changes in protein conformation induced by electromagnetic fields. *Bioelectromagnetics (Hoboken, NJ, United States)* **34**, 419-428, doi:10.1002/bem.21795 (2013).

13 Chen, W. Evidence of electroconformational changes in membrane proteins: Field-induced reductions in intra membrane nonlinear charge movement currents. *Bioelectrochemistry* **63**, 333-335, doi:10.1016/j.bioelechem.2003.12.007 (2004).

14 Singh, A., Munshi, S. & Raghavan, V. Effect of external electric field stress on gliadin protein conformation. *Proteomes* **1**, 25-39, 15, doi:10.3390/proteomes1020025 (2013).

15 Astrakas, L., Gousias, C. & Tzaphlidou, M. Electric field effects on chignolin conformation. *Journal of Applied Physics* **109**, 094702/094701-094702/094705, doi:10.1063/1.3585867 (2011).

16 Baker, E. G. *et al.* Local and macroscopic electrostatic interactions in single α-helices. *Nature Chemical Biology* **11**, 221-228, doi:10.1038/nchembio.1739 (2015).

17 Kim, S.-Y. Folding and unfolding simulations of a three-stranded beta-sheet protein. *Journal of Materials Science and Chemical Engineering* **4**, 13-17, doi:10.4236/msce.2016.41003 (2016).

18 Langer, A., Kaiser, W., Svejda, M., Schwertler, P. & Rant, U. Molecular Dynamics of DNA-Protein Conjugates on Electrified Surfaces: Solutions to the Drift-Diffusion Equation. *Journal of Physical Chemistry B* **118**, 597-607, doi:10.1021/jp410640z (2014).

19 Beleggia, M. & Zhu, Y. in *Modern Techniques for Characterizing Magnetic Materials* (ed Yimei Zhu) 267-326 (Kluwer Academic Publishers 2005).
20 Formanek, P. *et al.* Electron holography: applications to materials questions. *Annual Review of Materials Research* **37**, 539–588 (2007).
21 Thomas, J. M., Simpson, E. T., Kasama, T. & Dunin-Borkowski, R. E. Electron Holography for the Study of Magnetic Nanomaterials. *Acc. Chem. Res.* **41** 665-674 (2008).
22 Dunin-Borkowski, R. E. *et al.* Off-axis electron holography of exchange-biased CoFe/FeMn patterned nanostructures. . *J Appl. Phys.* **90**, 2899–2902 (2001).
23 Kawasaki, T., Endo, J., Matsuda, T., Osakabe, N. & Tonomura, A. Applications of holographic interference electron microscopy to the observation of biological specimens. *Journal of Electron Microscopy* **35**, 211-214 (1986).
24 Simon, P. *et al.* Electron holography of biological samples. *Micron* **39**, 229-256, doi:10.1016/j.micron.2006.11.012 (2008).
25 Namiot, V. A. How electron interference can be applied to analyzing the structure of small bio-objects and to fast reading of nucleotide sequences. *Biofizika* **53**, 538-543 (2008).
26 Fink, H. W., Schmid, H., Ermanntraut, E. & Schulz, T. Electron holography of individual DNA. *J. Opt. Soc. Am.* **A14**, 2168–2172. (1997).
27 Simon, P., Adhikari, R., Lichte, H., Michler, G. H. & Langela, M. Electron holography and AFM studies on styrenic block copolymers and a high impact polystyrene. . *J. Appl. Polym. Sci.* **96**, 1573–1583 (2005).
28 Ayache, J., Beaunier, L., Boumendil, J., Ehret, G. & Laub, D. *Sample Preparation Handbook for Transmission Electron Microscopy. Methodology.*, (Springer, 2010).
29 Matsumoto, T. Visualization of DNA in solution by Fraunhofer in-line electron holography: I. Simulation. *Optik (Jena, Germany)* **99**, 25-28 (1995).
30 Simon, P., Lichte, H., Wahl, R., Mertig, M. & Pompe, W. Electron holography of non-stained bacterial surface layer proteins. *Biochimica et Biophysica Acta, Biomembranes* **1663**, 178-187, doi:10.1016/j.bbamem.2004.03.005 (2004).
31 Latychevskaia, T., Longchamp, J.-N., Escher, C. & Fink, H.-W. Holography and coherent diffraction with low-energy electrons: A route towards structural biology at the single molecule level. *Ultramicroscopy* **159**, 395-402, doi:10.1016/j.ultramic.2014.11.024 (2015).
32 Longchamp, J.-N., Latychevskaia, T., Escher, C. & Fink, H.-W. Low-energy electron holographic imaging of individual tobacco mosaic virions. *Applied Physics Letters* **107**, 133101/133101-133101/133105, doi:10.1063/1.4931607 (2015).
33 Yu, W., He, X.-l., Liu, C. & Zhu, J.-q. Ptychographic iterative engine with incoherent illumination. *Wuli Xuebao* **64**, 244201/244201-244201/244207, doi:10.7498/aps.64.244201 (2015).
34 Reinhardt, J. *et al.* Beamstop-based low-background ptychography to image weakly scattering objects. *Ultramicroscopy* **173**, 52-57, doi:10.1016/j.ultramic.2016.11.005 (2017).
35 Hemonnot, C. Y. J. *et al.* X-rays Reveal the Internal Structure of Keratin Bundles in Whole Cells. *ACS Nano* **10**, 3553-3561, doi:10.1021/acsnano.5b07871 (2016).
36 Pan, A., Zhang, X.-f., Wang, B., Zhao, Q. & Shi, Y.-s. Experimental study on three-dimensional ptychography for thick sample. *Wuli Xuebao* **65**, 014204/014201-014204/014216, doi:10.7498/aps.65.014204 (2016).
37 Donnelly, C. *et al.* High-resolution hard x-ray magnetic imaging with dichroic ptychography. *Physical Review B* **94**, 064421/064421-064421/064429, doi:10.1103/PhysRevB.94.064421 (2016).
38 Rodriguez, J. A., Xu, R., Chen, C.-C., Zou, Y. & Miao, J. Oversampling smoothness: an effective algorithm for phase retrieval of noisy diffraction intensities. *Journal of Applied Crystallography* **46**, 312-318, doi:10.1107/s0021889813002471 (2013).

39 Kobayashi, A. *et al.* Specimen preparation for cryogenic coherent X-ray diffraction imaging of biological cells and cellular organelles by using the X-ray free-electron laser at SACLA. *Journal of Synchrotron Radiation* **23**, 975-989, doi:10.1107/s1600577516007736 (2016).
40 Hoyer, P. *et al.* Breaking the diffraction limit of light-sheet fluorescence microscopy by RESOLFT. *Proceedings of the National Academy of Sciences of the United States of America* **113**, 3442-3446, doi:10.1073/pnas.1522292113 (2016).
41 Shibata, N. *et al.* Imaging of built-in electric field at a p-n junction by scanning transmission electron microscopy. *Scientific Reports* **5**, 10040, doi:10.1038/srep10040 (2015).
42 Majert, S. & Kohl, H. High-resolution STEM imaging with a quadrant detector-Conditions for differential phase contrast microscopy in the weak phase object approximation. *Ultramicroscopy* **148**, 81-86, doi:10.1016/j.ultramic.2014.09.009 (2015).
43 Denneulin, T., Houdellier, F. & Hytch, M. Differential phase-contrast dark-field electron holography for strain mapping. *Ultramicroscopy* **160**, 98-109, doi:10.1016/j.ultramic.2015.10.002 (2016).
44 de Jonge, N. & Ross, F. M. Electron microscopy of specimens in liquid. *Nature Nanotechnology* **6**, 695-704, doi:10.1038/nnano.2011.161 (2011).
45 Peckys, D. B., Dukes, M. J., Ring, E. A., Piston, D. W. & de Jonge, N. Imaging specific protein labels on eukaryotic cells in liquid with scanning transmission electron microscopy. *Microscopy Today* **19**, 16, 18-20, doi:10.1017/s1551929511000903 (2011).
46 Peckys, D. B. & de Jonge, N. Liquid Scanning Transmission Electron Microscopy: Imaging Protein Complexes in their Native Environment in Whole Eukaryotic Cells. *Microscopy and Microanalysis* **20**, 346-365, doi:10.1017/s1431927614000099 (2014).
47 Kashyap, S., Woehl, T. J., Liu, X., Mallapragada, S. K. & Prozorov, T. Nucleation of Iron Oxide Nanoparticles Mediated by Mms6 Protein In Situ. *ACS Nano* **8**, 9097-9106, doi:http://dx.doi.org/10.1021/nn502551y (2014).
48 Wang, C., Qiao, Q., Shokuhfar, T. & Klie, R. F. High-Resolution Electron Microscopy and Spectroscopy of Ferritin in Biocompatible Graphene Liquid Cells and Graphene Sandwiches. *Advanced Materials (Weinheim, Germany)* **26**, 3410-3414, doi:10.1002/adma.201306069 (2014).
49 Dukes, M. J., Ramachandra, R., Baudoin, J.-P., Gray Jerome, W. & de Jonge, N. Three-dimensional locations of gold-labeled proteins in a whole mount eukaryotic cell obtained with 3 nm precision using aberration-corrected scanning transmission electron microscopy. *Journal of Structural Biology* **174**, 552-562, doi:10.1016/j.jsb.2011.03.013 (2011).
50 Dukes, M. J. *Scanning transmission electron microscopy of tagged proteins in whole eukaryotic cells*, (2011).
51 Woehl, T. J. *et al.* Correlative Electron and Fluorescence Microscopy of Magnetotactic Bacteria in Liquid: Toward In Vivo Imaging. *Scientific Reports,* **4**, 6854, doi:10.1038/srep06854 (2014).
52 Woehl, T. J. & Prozorov, T. in *Liquid Cell Electron Microscopy* (eds Frances Ross & Niels de Jonge) Ch. 23, 476-500 (Cambridge University Press, 2017).
53 Shirai, M. *et al.* In situ electron holographic study of Ionic liquid. *Ultramicroscopy* **146**, 125-129, doi:10.1016/j.ultramic.2014.08.003 (2014).
54 Dunin-Borkowski, R. E. *et al.* Magnetic microstructure of magnetotactic bacteria by electron holography. *Science* **282**, 1868-1870 (1998).
55 Dunin-Borkowski, R. E. *et al.* Off-axis electron holography of magnetotactic bacteria: magnetic microstructure of strains MV-1 and MS-1. *Eur. J. Mineral.* **13**, 671–684 (2001).
56 Simpson, E. T. *et al.* Magnetic induction mapping of magnetite chains in magnetotactic bacteria at room temperature and close to the Verwey transition using electron holography. *Journal of Physics: Conference Series* **17**, 108-121, doi:10.1088/1742-6596/17/1/017 (2005).

57 Staniland, S., Ward, B., Harrison, A., van der Laan, G. & Telling, N. Rapid magnetosome formation shown by real-time x-ray magnetic circular dichroism. *Proc. Natl. Acad. Sci.* **104**, 19524-19528, doi:10.1073/pnas.0704879104 (2007).
58 Fdez-Gubieda, M. L. *et al.* Magnetite biomineralization in Magnetospirillum gryphiswaldense: time-resolved magnetic and structural studies. *ACS Nano* **7**, 3297-3305, doi:10.1021/nn3059983 (2013).
59 Zhu, X. H. *et al.* in *AIP Conference Proceedings [0094-243X]*. 020002 (American Institute of Physics).
60 Midgley, P. A. & Dunin-Borkowski, R. E. Electron tomography and holography in materials science. *Nat. Mater.* **8**, 271-280, doi:doi: 10.1038/nmat2406 (2009).
61 Devouard, B. *et al.* Magnetic from magnetotactic bacteria: size distributions and twinning. *American Mineralogist* **83**, 1387-1398 (1998).
62 Kasama, T., Dunin-Borkowski, R. E. & Beleggia, M. in *Holography— Different Fields of Application* (ed F. A. Monroy Ramírez) 53-80 (InTech, 2011).
63 Grogan, J. M., Schneider, N. M., Ross, F. M. & Bau, H. H. Bubble and Pattern Formation in Liquid Induced by an Electron Beam. *Nano Letters* **14**, 359-364, doi:10.1021/nl404169a (2014).
64 Schneider, N. M. *et al.* Electron-Water Interactions and Implications for Liquid Cell Electron Microscopy. *Journal of Physical Chemistry C* **118**, 22373-22382, doi:10.1021/jp507400n (2014).
65 Mirsaidov, U., Ohl, C.-D. & Matsudaira, P. A direct observation of nanometer-size void dynamics in an ultra-thin water film. *Soft Matter* **8**, 7108-7111, doi:10.1039/c2sm25331c (2012).
66 Komeili, A., Vali, H., Beveridge, T. J. & Newman, D. K. Magnetosome vesicles are present before magnetite formation, and MamA is required for their activation. . *P. Natl. Acad. Sci. USA* **101**, 3839-3844 (2004).
67 Lang, C. & Schueler, D. Biogenic nanoparticles: production, characterization, and application of bacterial magnetosomes. *Journal of Physics: Condensed Matter* **18**, S2815-S2828 (2006).
68 Schueler, D. Nano crystals for magnetic field orientation. Biomineralization of magnetosomes in bacteria. *BIOspektrum* **11**, 291-294 (2005).
69 Matsunaga, T., Sakaguchi, T. & Tadokoro, F. Magnetite formation by a magnetic bacterium capable of growing aerobically. *Applied Microbiology and Biotechnology* **35**, 651-655, doi:10.1007/bf00169632 (1991).
70 Bazylinski, D. A. & Frankel, R. B. Magnetic iron oxide and iron sulfide minerals within microorganisms: Potential biomarkers. *Biomineralization (2nd Edition)*, 17-43 (2004).
71 Prozorov, R. *et al.* Magnetic irreversibility and Verwey transition in nano-crystalline bacterial magnetite. *Phys. Rev. B. Cond. Mat.* **76**, 054406 054401-054410 (2007).
72 Scheffel, A. *et al.* An acidic protein aligns magnetosomes along a filamentous structure in magnetotactic bacteria. *Nature* **440**, 110-114 (2005).
73 Komeili, A., Li, Z., Newman, D. K. & Jensen, G. J. Magnetosomes are cell membrane invaginations organized by the actin-like protein MamK. *Science* **311**, 242-245 (2006).
74 McCartney, M. R., Lins, U., Farina, M., Buseck, P. R. & Frankel, R. B. Magnetic microstructure of bacterial magnetite by electron holography. *Eur. J. Mineral.* **13**, 685-689, doi:10.1127/0935-1221/2001/0013-0685 (2001).
75 Posfai, M., Kasama, T. & Dunin-Borkowski, R. E. Biominerals at the nanoscale: transmission electron microscopy methods for studying the special properties of biominerals. *EMU Notes in Mineralogy* **14**, 375-433 (2013).
76 Sellner, B. & Kathmann, S. M. A matter of quantum voltages. *Journal of Chemical Physics* **141**, 18C534/531-518C534/513, doi:10.1063/1.4898797 (2014).

77 Kathmann, S. M., Kuo, I. F. W. & Mundy, C. J. Electronic Effects on the Surface Potential at the Vapor-Liquid Interface of Water. *Journal of the American Chemical Society* **130**, 16556-16561, doi:10.1021/ja802851w (2008).
78 Kathmann, S. M., Kuo, I. F. W., Mundy, C. J. & Schenter, G. K. Understanding the surface potential of water. *Journal of Physical Chemistry B* **115**, 4369-4377, doi:10.1021/jp1116036 (2011).
79 Kathmann, S. M., Sellner, B., Alexander, A. J. & Valiev, M. Beyond classical theories. *AIP Conference Proceedings* **1527**, 109-112, doi:10.1063/1.4803215 (2013).
80 Harscher, A. & Lichte, H. in *ICEM14*. (eds H.A. Calderon Benavides & M. J. Yacaman) 553-554 (Institute of Physics Publishing,, 1998).
81 Simon, P. *et al.* Electron holography of organic and biological materials. *Advanced Materials (Weinheim, Germany)* **15**, 1475-1481, doi:10.1002/adma.200301645 (2003).
82 Heyen, U. & Schüler, D. Growth and magnetosome formation by microaerophilic Magnetospirillum strains in an oxygen-controlled fermentor. *Appl Microbiol Biotechnol* **61**, 536-544, doi:10.1007/s00253-002-1219-x (2003).
83 Faivre, D., Menguy, N., Posfai, M. & Schüler, D. Environmental parameters affect the physical properties of fast-growing magnetosomes. *American Mineralogist* **93**, 463-469, doi:10.2138/am.2008.2678 (2008).
84 Firlar, E., Perez Gonzalez, T., Olszewska, A., Faivre, D. & Prozorov, T. Following Iron Speciation in the Early Stages of Magnetite Magnetosome Biomineralization. *J. Mater. Res. Focus issue on Biomineralization and Biomimetics* **31**, 547-555 (2016).

1 Figure Legends

Figure 1. Schematic diagrams showing the experimental setup in the present study. (A) TEM imaging with a fluid cell (not to scale). The microfluidic chamber consists of two silicon microchips supporting two 50-nm-thick electron-transparent SiN membranes. Cells of *M. Magneticum* are attached to the top SiN window and imaged using an incident electron beam in a thin liquid layer. (B) Off-axis electron holography using a fluid cell (adapted from [60]).

Figure 2. Electron holography and associated analysis of a hydrated bacterial cell. (A) Off-axis electron hologram of a hydrated bacterial cell between two SiN membranes. The scale bar is 200 nm. The magnified region in the inset shows well-resolved interference fringes with a spacing of ~5.6 nm. (B) Wrapped phase image showing a $0 - 2\pi$ range of phase values presented in the image and (C) amplitude image of the bacterial cell in (A). (D-F) Off-axis electron holograms acquired in (D) the initial state, (E) after tilting by +75° and applying a magnetic field in the electron beam direction and (F) after tilting by -75° and applying a magnetic field in the electron beam direction. The scale bars are 100 nm. The spacing of the holographic interference fringes is ~5.7 nm. Examples of electron-beam-induced changes to the specimen include the progression of voids outlined in yellow and red. (G) Magnetic induction map of the magnetite chain in the bacterial cell reconstructed from the dashed area in (F). The black phase contours were formed from the magnetic contribution to the recorded phase shift and have a spacing of 0.098±0.001 radians. The outlines of the individual magnetite nanocrystals are marked in white. The direction of the measured projected in-plane magnetic induction is shown using arrows and colors, according to the color wheel shown in the inset. The in-plane component of the magnetic field applied to the specimen before recording the holograms in (E) and (F) is labelled FD and marked by blue and red arrows. (H) Profile of the magnetic contribution to the phase shift across the magnetite particle shown in (G) denoted by a red dashed line, yielding a saturation magnetic induction of 0.58 ± 0.1 T.

Figure 3. Electron holography and visualized magnetization of a magnetite nanocrystal chain. (A) Off-axis electron hologram of a magnetite nanocrystal chain that had been released from a ruptured bacterium, showing well-resolved holographic interference fringes with a spacing of ~6.2 nm. The scale bar is 100 nm. (B) Corresponding magnetic induction map. The phase contour spacing is 0.31 ±0.001 radians. The in-plane component of the magnetic field applied to the specimen before recording the holograms is labelled FD and marked by blue and red arrows. (C) Profile of the magnetic contribution to the phase shift across the magnetite particle shown in (B) denoted by a red dashed line, yielding a saturation magnetic induction of 0.63 ± 0.1 T.

Figure 4. Electron holography and associated analysis of regions of liquid. (A, B) Off-axis electron holograms recorded from the middle of the fluid cell and from a liquid front that partially covers the SiN window, respectively. The scale bars are 200 nm in (A) and 300 nm in (B). The magnified regions in the insets show well-resolved interference fringes with a spacing of ~6.2 nm. (C) Off-axis electron hologram recorded from a droplet of liquid in the fluid cell (~1200 nm in diameter and assumed to be ~800 nm in height) with a holographic interference fringe spacing of ~5.7 nm. The scale bar is 200 nm. (D) Radial average of intensity of the droplet shown in (C). (E) Amplitude image, (F) t/λ profile across the droplet, and (G) phase profile across the droplet reconstructed using off-axis electron holography. The scale bar in (E) is 200 nm.

Figure 5. Comparison of off-axis electron holograms recorded using two cameras. Off-axis electron holograms recorded from the fluid cell using (A) a conventional CCD camera and (B) a K2 direct electron detector. A 6 s acquisition time was used in each case.

Figures

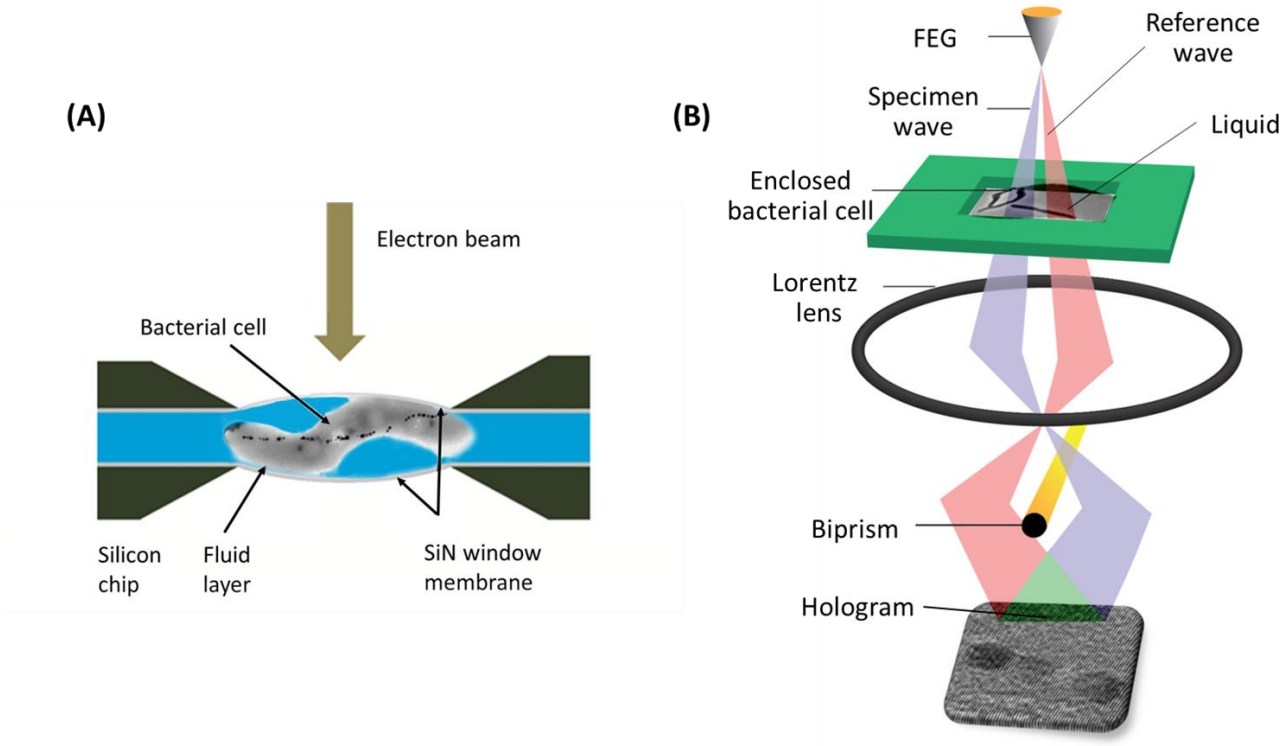

Figure 1.

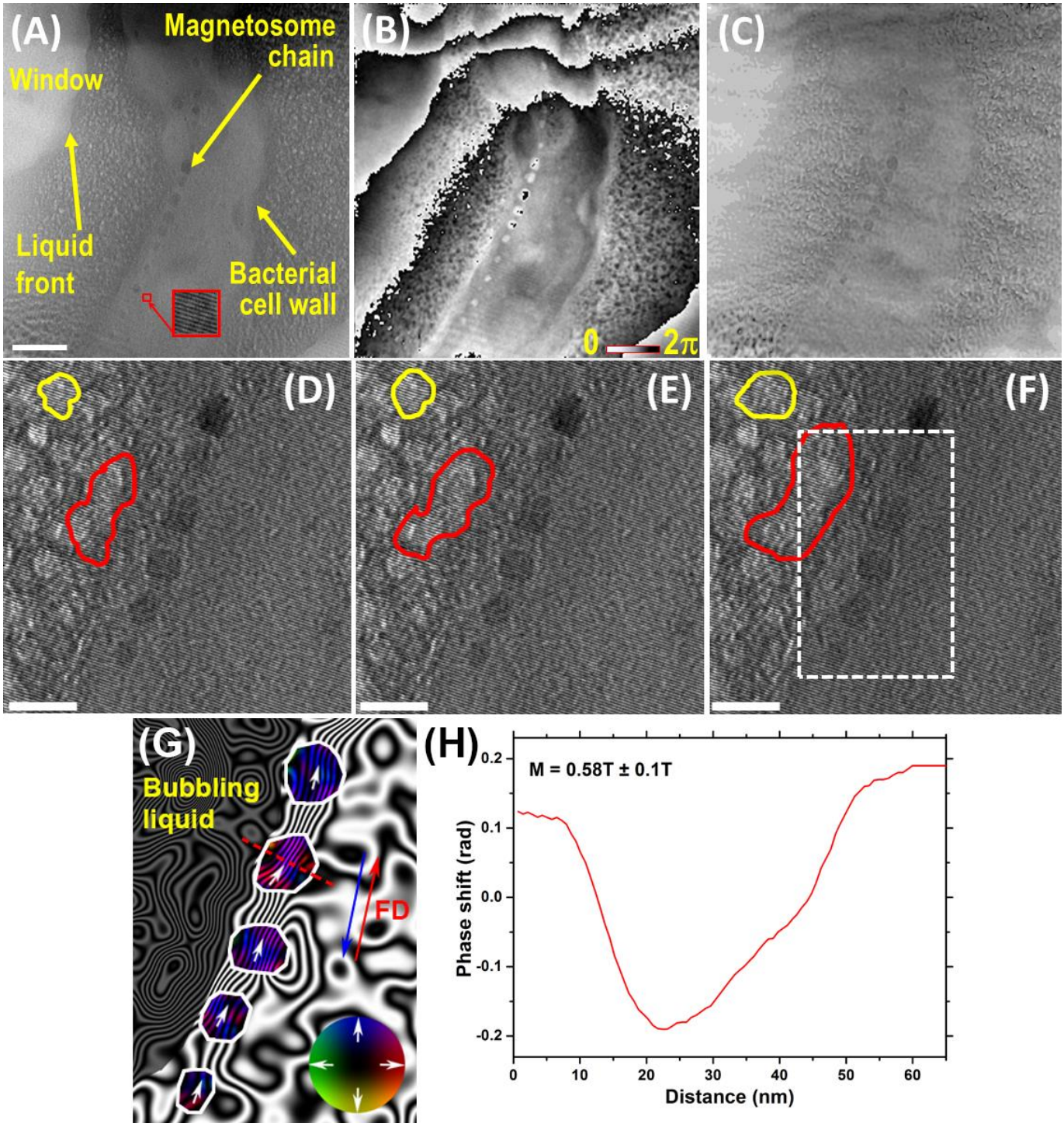
(A)
Magnetosome chain
Window
Liquid front
Bacterial cell wall
(B)
0
2π
(C)
(D)
(E)
(F)
(G)
Bubbling liquid
FD
(H)
M = 0.58T ± 0.1T
Phase shift (rad)
0.2
0.1
0.0
-0.1
-0.2
0
10
20
30
40
50
60
Distance (nm)

Figure 2.

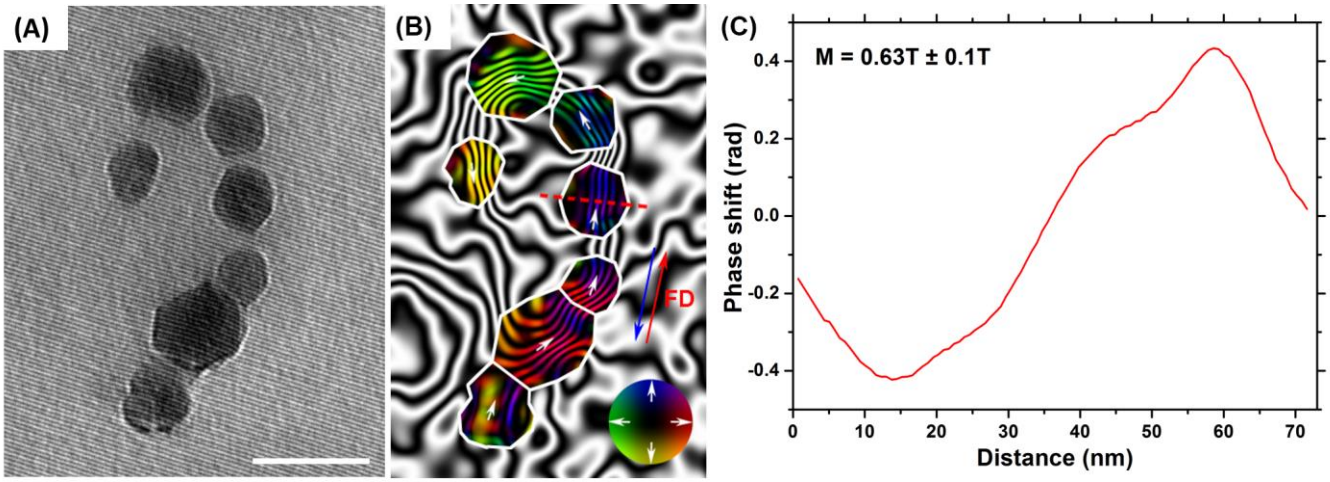
(A)
(B)
FD
(C)
M = 0.63T ± 0.1T
Phase shift (rad)
0.4
0.2
0.0
-0.2
-0.4
0
10
20
30
40
50
60
70
Distance (nm)

Figure 3.

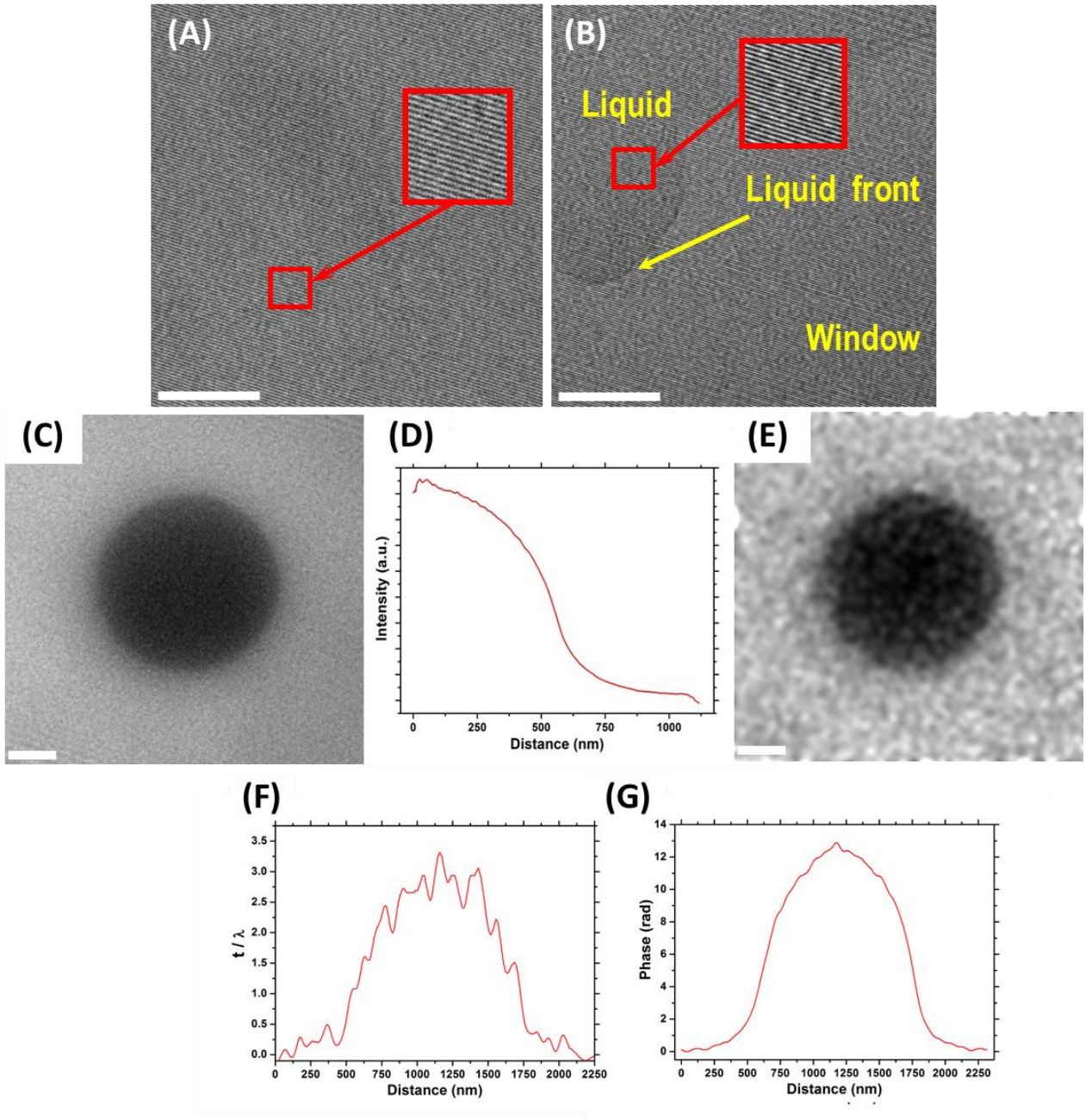
(A)
(B)
Liquid
Liquid front
Window
(C)
(D)
Intensity (a.u.)
Distance (nm)
(E)
(F)
t / λ
Distance (nm)
(G)
Phase (rad)
Distance (nm)

Figure 4.

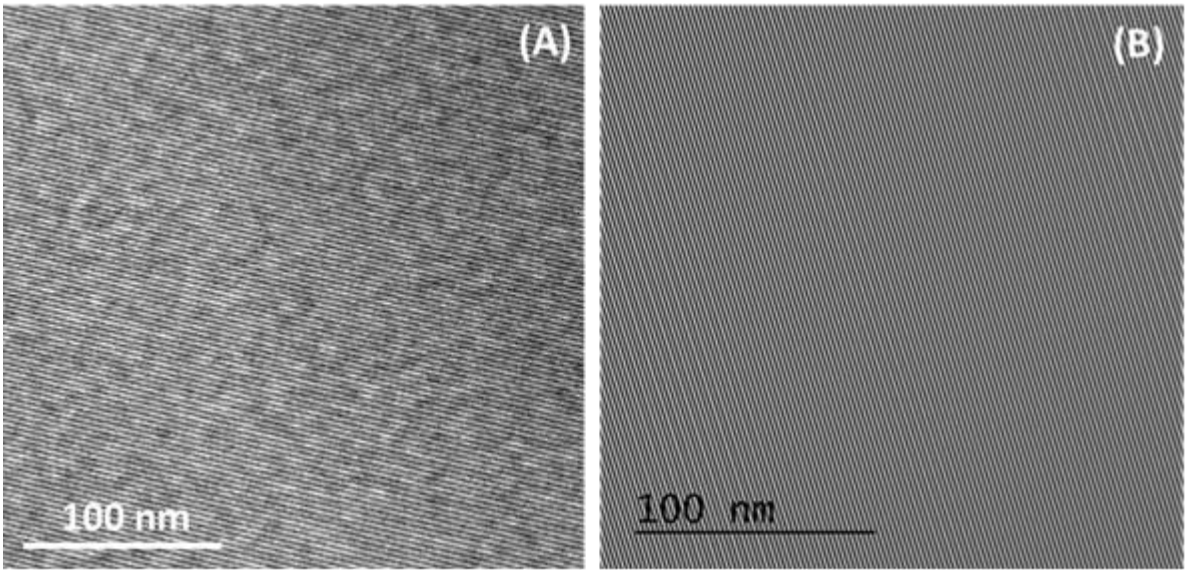

Figure 5.